Three dimensional (3D) microstructure-based finite element modeling of Al-SiC nanolaminates using focused ion beam (FIB) tomography

Carl R. Mayer [a], Jon Molina-Aladareguia [b], Nikhilesh Chawla [a,*]

[a] Materials Science and Engineering, Arizona State University, Tempe, AZ 85287-6106, United States
[b] IMDEA Materials Institute, c/Eric Kandel 2, Getafe, Madrid 28906, Spain

ARTICLE INFO

ABSTRACT

Al-SiC nanolaminate composites show promise as high performance coating materials due to their combination of strength and toughness. Although a significant amount of modeling effort has been focused on materials with an idealized flat nanostructure, experimentally these materials exhibit complex undulating layer geometries. This work utilizes FIB tomography to characterize this nanostructure in 3D and finite element modeling to determine the effect that this complex structure has on the mechanical behavior of these materials. A sufficiently large volume was characterized such that a 1×2 µm micropillar could be generated from the dataset and compared directly to experimental results. The mechanical response from this nanostructure was then compared to pillar models using simplified structures with perfectly flat layers, layers with sinusoidal waviness, and layers with arc segment waviness. The arc segment based layer geometry showed the best agreement with the experimentally determined structure, indicating it would be the most appropriate geometry for future modeling efforts.

© 2016 Elsevier Inc. All rights reserved.

1. Introduction

Laminated composite structures have long been used to tailor the properties of materials for specific applications by varying the composition, scale, and volume fraction of the individual phases used. By decreasing the thickness of the layers to the nanoscale, very interesting mechanical properties can be obtained, such as high strength, toughness, and wear resistance [1–6]. Additionally, these nanolaminate composites have been shown to exhibit unique functional properties such as biocompatibility [7], and enhanced optical properties [8].

An ever growing body of literature has focused on these materials. In an effort to understand the underlying deformation mechanisms, several papers have dealt with modeling approaches over a range of length scales to better understand different aspects of the mechanical behavior. These methods have included molecular dynamics (MD) simulations [9, 10] which allows detailed investigation of interfaces and dislocations but with very limited size and time scales, molecular statistics (MS) simulations [11] which provides similar information as MD simulations with reduced computation time, dislocation dynamics (DD) simulations [12] which can be used to determine the transitions in dislocation behavior seen in multilayers as a function of layer thickness, and finite element (FE) modeling [13–15] which can determine how the stresses

and strains are distributed within heterogeneous structures even under complex loading conditions such as indentation.

The vast majority of this literature assumes a perfectly flat layer structure [6,11,14,15], which is not representative of the actual nanostructure, as seen in Fig. 1. The waviness in the layers is a byproduct of
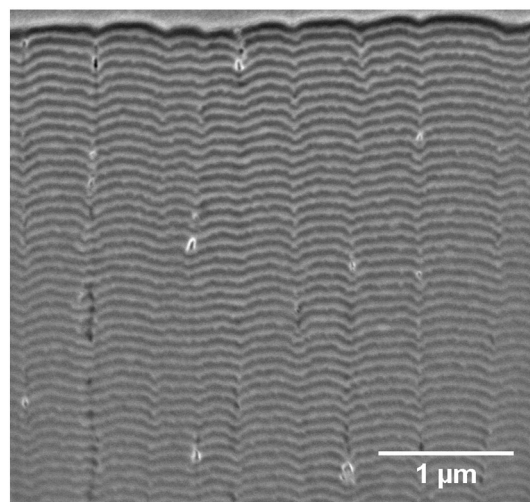

Fig. 1. SEM image of nanolaminate nanostructure, showing significant waviness in the deposited layers.

* Corresponding author at: 501 E. Tyler Mall, ECG 303, Arizona State University, Tempe, AZ 85287-6106, United States.
   E-mail address: nchawla@asu.edu (N. Chawla).

the deposition process and has been observed experimentally in a number of multilayer systems [16–19]. This type of columnar growth structure occurs because any small amount of roughness is exaggerated upon application of another layer, eventually leading to shading and porosity [20]. Experimentally this difference in the nanostructure results in significant changes in the observed deformation behavior. This is especially apparent in recent work using micropillar compression [21], where waviness in the layers was shown to both allow buckling of the layers to occur at much lower stresses and also hinder shear deformation within individual layers. Additionally under nanoindentation loading, the increased waviness was shown make the measured moduli more isotropic [18] and the stresses more localized [18,19]. Some more recent studies have begun implementing non-ideal structures to account for this, for example layers with sinusoidal waviness [13,18,21,22] or arc segment waviness [19].

Finite element (FE) modeling using experimentally obtained microstructures can provide more accurate results as well as meaningful insights into the deformation behavior compared to simple model

Fig. 3. Pillar models used with flat, cosine, arc segment, and FIB derived nanostructures (respectively from left to right). Al layers are depicted in green while SiC layers are depicted in gray. (For interpretation of the references to colour in this figure legend, the reader is referred to the web version of this article.)

systems [23–26]. A variety of experimental methods are available to characterize materials in three dimensions (3D). These techniques range from relatively coarse techniques such as optical sectioning
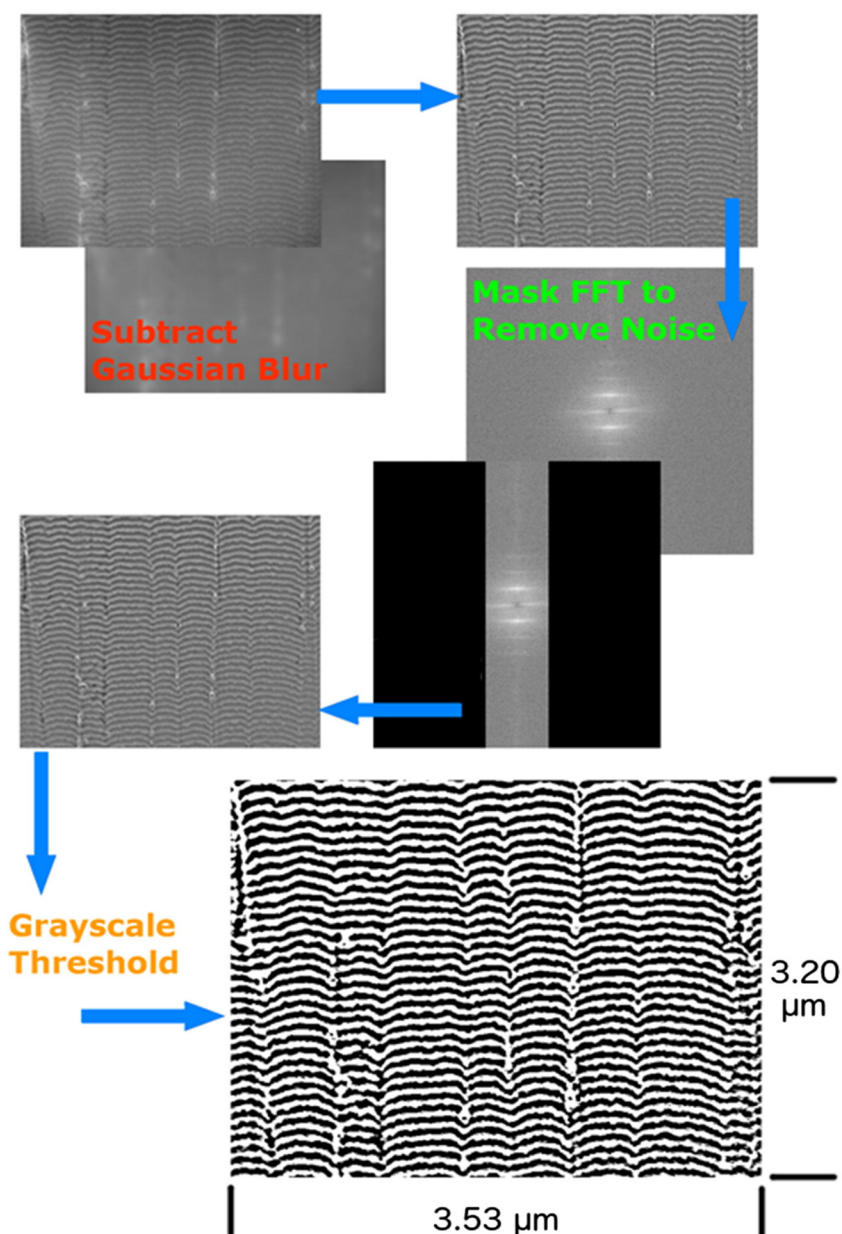

Fig. 2. Outline of the image processing steps used to segment the Al and SiC phases from the raw images.
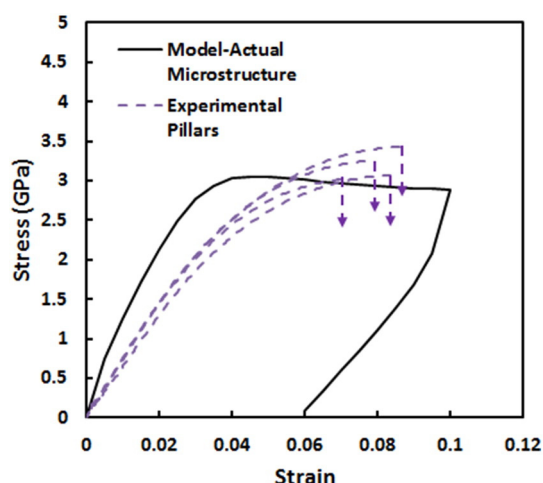
Fig. 4. Comparison of experimental pillar compression response [12] to the modeled response using the FIB tomography derived nanostructure.

microscopy [26], to x-ray computed tomography with sub-micrometer resolution [27], and to atom probe tomography with individual atom location attainable [28]. The length scales of interest in this study of nanolaminate materials (requiring nanometer scale resolution over tens of cubic micrometers of volume) makes focused ion beam (FIB) tomography the most appropriate compromise between the required resolution and volume of material which needs to be characterized. This technique utilizes a dual beam FIB/SEM to image the structure with a high resolution SEM while sequentially removing thin slices of material (typically on the order of tens of nanometers) with the FIB [29]. The

depth resolution of this technique is determined by the slice thickness, which in theory is limited by the resolution of the ion beam and can therefore achieve resolutions at the nanometer scale, although, in the interest of efficiency, larger slices on the order of tens of nanometer are often removed to reduce the time required. Additionally, with FIB tomography volumes as large as tens of cubic micrometers of material can be characterized. This volume is large enough to allow a 1 μm diameter by 2 μm height pillar to be cropped from the reconstructed volume and used in simulations, allowing direct comparison to experimental compression experiments carried out in previous work [21].

For the case of these nanolaminate materials, the amplitude and wavelength of the waviness varies from sample to sample depending on the exact processing parameters, layer thicknesses, and materials used, making it impractical to experimentally determine the microstructure in 3D for every sample. Thus, the aim of this work is to determine how appropriate perfectly flat, sinusoidal, and arc segment nanostructures are for modeling the deformation of these laminate structures. By comparing the simulated mechanical responses of each of these simplified structures to the simulated response from experimentally determined structure obtained using FIB tomography, as well as experimental pillar compression results from previous work [21], we are able to determine which idealized structure provides the most accurate approximation of both the constitutive stress-strain relations as well as the localization of deformation within each structure.

2. Materials and methods

The metal-ceramic nanolaminate composites were fabricated using an automated magnetron sputtering procedure, the details of which are given elsewhere [9,10]. The samples used in this study consisted of alternating layers of Al and SiC, each having an individual layer
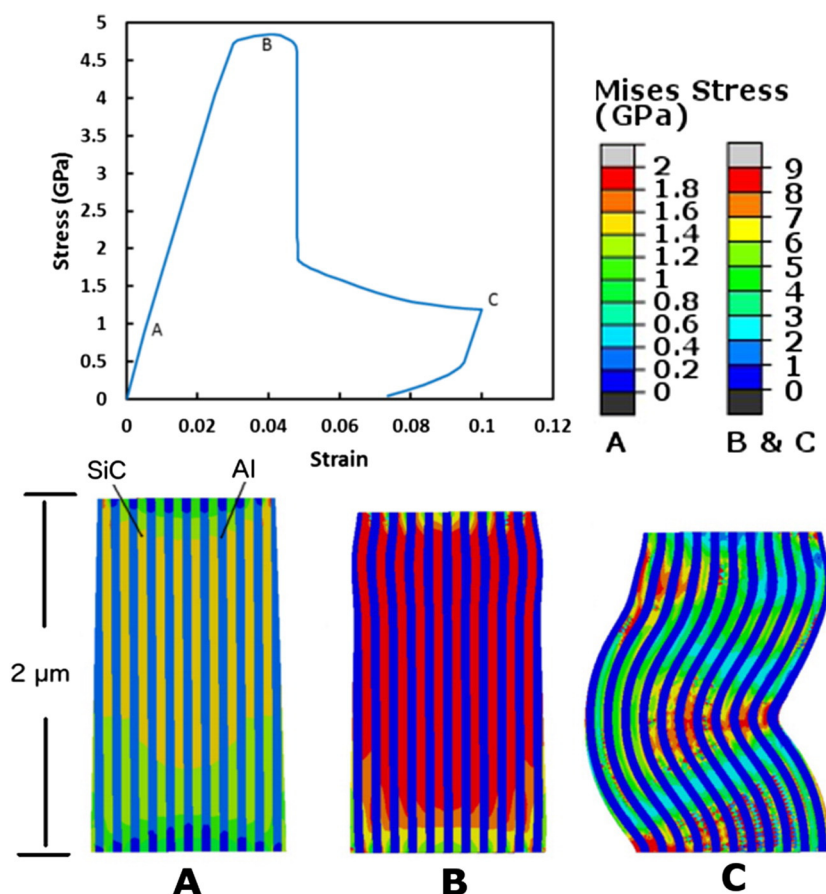

Fig. 5. Modeled stress strain response of the flat nanostructure pillar. Von Mises stress contours correspond to the points indicated on the curve.

thickness of approximately 50 nm. These layers were deposited sequentially until a total multilayer thickness of approximately 15 μm was obtained (approximately 300 layers).

FIB tomography was carried out in a dual beam FIB/SEM (Nova200, FEI, Hillsboro, OR). Cross-sections approximately 5 μm × 5 μm in size were imaged following each milling step. Slices of 80 nm each were removed in each step using the FIB. Ion beam images normal to the sample surface were used to measure the distance from the cross section to a reference fiduciary mark, thereby providing an accurate measure of the slice thickness. The cross section cut using the FIB was then imaged at 52° relative to the surface normal. The images were scaled along the cross section height in order to compensate for this imaging angle. A total of 23 slices were imaged for a total depth of 1.8 μm. These slices were then manually aligned using the Avizo Fire (VSG, Burlington, MA) software. A volume of 3.2 μm by 3.5 μm by 1.8 μm was cropped from these aligned slices in order to both remove the misaligned edges as well as provide a volume of material with maximum contrast.

Before the 3D volume characterized using FIB tomography could be utilized in a FE model, the Al and SiC phases needed to be segmented in each of the 2D slices. As the contrast differences in the raw images were not adequate for grayscale thresholding immediately, a variety of image manipulations were implemented (Image J, Bethesda, MD) in order to improve the image quality, as shown in Fig. 2. First, in order to remove the background contrast variations, a Gaussian blur was applied to the image and then this blurred image was subtracted from the original. The radius of this Gaussian blur was adjusted to the minimum size where any feature of interest is not visible in the blurred image, in this case 50 nm. Since the features of interest in this case were the horizontal layered structure, a mask was applied to the Fourier transform of the

image in order to remove much of the noise without affecting the horizontal features. This process provided images which were able to be segmented using standard grayscale thresholding. Due to contrast differences, areas immediately surrounding pores in the material required manual adjustment to ensure layer continuity. As the slice thickness was much larger than the x and y pixel size, the image stack resulted in non-cubic voxels. In order to obtain uniform cubic voxels, the 3D volume was resampled with layer positions interpolated linearly between the slices. Avizo Fire was then used to generate a 3D solid tetrahedral mesh of the structure.

Three simplified nanostructure geometries, with layers consisting of either flat, cosine or arc sections, were developed in order to approximate the experimental structure. Using a single cross sectional image, the average amplitude and wavelength of the undulations were measured to be 50 nm and 475 nm, respectively. Equivalent amplitude and wavelength values were used while generating the cosine and arc section based geometries.

In order to mimic experimental pillar compression studies, 1 μm diameter by 2 μm height pillars were cropped from each of the geometries as seen in Fig. 3. A 2° taper was also incorporated in the pillar models, as seen experimentally [21]. In each of the models the layers were oriented parallel to the loading axis, as this orientation showed the strongest dependence on layer waviness, as per previous studies [18,21].

The deformation of the micropillars was simulated by FE modeling using the commercial software Abaqus (Abaqus, v. 6.12, Dassault Systems Simulia Corp., Providence, RI). All the pillar models were meshed using 4-node tetrahedral elements (C3D4). To determine the number of elements required for mesh convergence, the cosine geometry mesh was iteratively refined in ~100,000 element steps until deviations
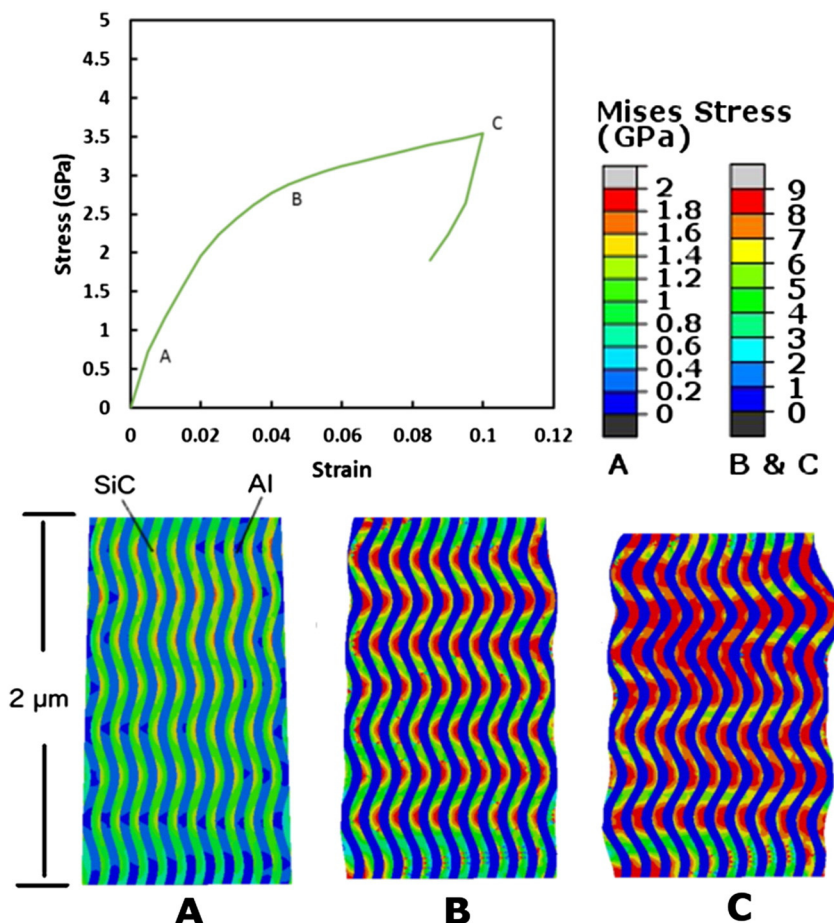

Fig. 6. Modeled stress strain response of the cosine nanostructure pillar. Von Mises stress contours correspond to the points indicated on the curve.

in the peak load were determined to be less than 1% from the previous iteration, which occurred at ~600,000 elements. This element count was used for the cos, arc and flat geometries, while the FIB derived mesh generated from the Avizo Fire program contained ~1,000,000 elements. The bottom surface of the pillar was completely constrained while the top surface was constrained in the x and z dimensions and displaced as a function of time in the y dimension in order to induce the deformation. Displacement was carried out at a rate of 2 nm/s to a maximum of 200 nm, corresponding to an initial strain rate of 0.001 s^{-1} and a maximum strain of 0.1. During loading, this set of constraints is analogous to displacement controlled micropillar compression with a rigid indenter and high contact friction between the indenter and pillar top. A deformable base material was excluded from all models because this additional source of compliance has already been accounted for using the Sneddon correction [6] in the experimental results being used for comparison [21].

The constitutive behavior used for the Al and SiC phases has been utilized in previous studies [15,30] and was approximated from the results of indentations made on 1 μm thick monolithic films of each phase, using the same deposition parameters. For the aluminum phase, the elastic modulus and Poisson's ratio were 59 GPa and 0.33, respectively, with an initial yield point of 200 MPa. A piecewise hardening behavior following yield was used with linear hardening between (stress, plastic strain) points of (200 MPa, 0), (300 MPa, 0.5), and (400 MPa, 3), followed by perfectly plastic behavior. For the SiC phase, the elastic modulus and Poisson's ratio was 277 GPa and 0.18, respectively. A yield point of 8770 MPa was chosen, followed by perfect plasticity. Although the brittle SiC is not expected to undergo significant plasticity experimentally, unrealistically high stresses occur using purely elastic behavior due to the lack of fracture incorporated into the models. Therefore, allowing

perfectly plastic deformation after a high yield (essentially fracture) point estimated from the indentation hardness allows for a closer approximation of the actual behavior. The boundaries between the Al and SiC phases are modeled as perfect interfaces, an assumption which has been shown to provide strong agreement with experimental results at room temperature [14].

3. Results and discussion

A comparison of experimental pillar compression curves with the simulated result from the FIB determined microstructure is shown in Fig. 4. The model shows very good agreement with the experimental data, with the maximum stress in the model falling within the range reported for the experimental pillars. One notable difference between the model and the experimental pillars is that the measured modulus in the experimental stress strain curves is much lower than the modeled behavior. This lower apparent modulus has also been seen in previous studies when comparing the modulus calculated using the stress strain curve and the continuous stiffness measurement (CSM) based modulus [6]. The root of this difference is extraneous contributions to the compliance. These can include underestimates of the Sneddon correction to the sink in effect, additional compliance in the instrument load frame, slight misalignments or surface asperities on the pillar top causing imperfect contact [6,31]. Due to the electrostatic actuation of the indenter tip, the experimental pillar compression results are inherently load controlled, resulting in large displacement jumps at fracture events or plastic instabilities. Therefore, for the experimental data, failure is defined at the first instance of a negative hardening rate and denoted by a downward arrow.
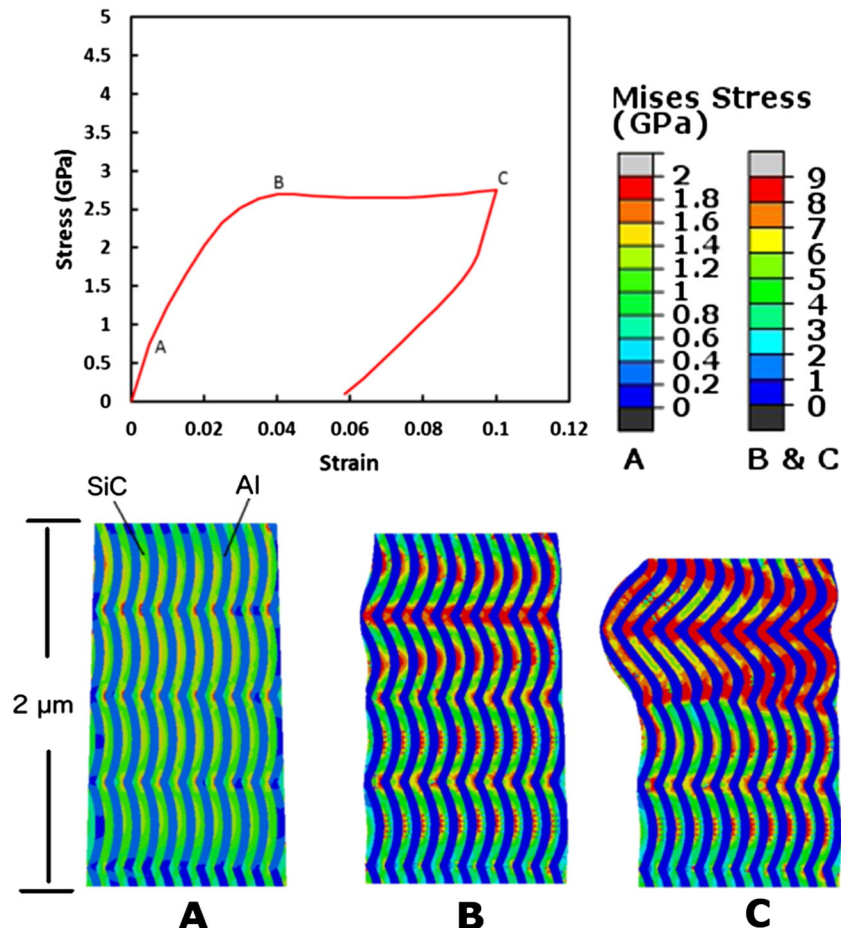

Fig. 7. Modeled stress strain response of the arc segment nanostructure pillar. Von Mises stress contours correspond to the points indicated on the curve.
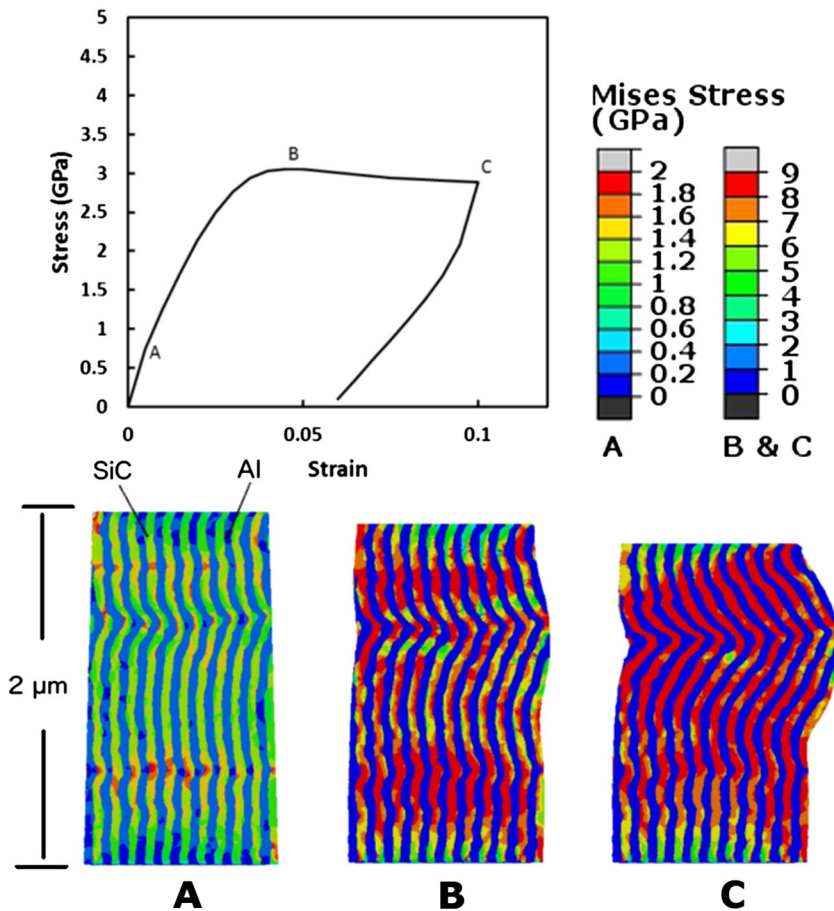
Fig. 8. Modeled stress strain response of the FIB derived nanostructure pillar. Von Mises stress contours correspond to the points indicated on the curve.

Stress strain curves and corresponding frames showing the Von Mises stress contours for the FIB, flat, cosine and arc segment structures are shown in Figs. 5–8, respectively. Videos of the deformation are provided in the supplemental material. The fully deformed pillars using the experimental and arc segment structures (Fig. 7 and Fig. 8(c)) show significant buckling of the layers in a single localized region. This is also observed experimentally [21], although the lateral constraint imposed on the top surface of the modeled pillars likely reduces this effect. Directly comparing the stress strain curves from each of the models indicates

that, based on the overall mechanical response, the arc segment based nanostructure is the best approximation of the experimentally determined structure, as seen in Fig. 9.

In addition to the overall mechanical response quantified by the stress strain curves, it is also important to determine which model best approximates the localization of stresses in the structure. This is especially relevant to fracture processes, where the high local stresses can drive flaw propagation. In order to quantify this localization, the distribution of stresses along the loading axis (S22) was quantified at a strain of 0.005, which is within the elastic regime. For each of the models, the distribution of the stresses in the SiC elements was calculated as shown in Fig. 10. In order to quantify how well the localization in the FIB determined structure is reproduced by each of the simplified geometries, the R^2 parameter was used to determine the goodness of fit. The R^2 values for the flat, cosine, and arc segment structures were determined to be -1.67, 0.86, and 0.95, respectively. This indicates that the arc segment model approximates the localization of stresses the most accurately as well.

It is also interesting to note where the stresses are being localized within the structure. In each of the structures incorporating waviness, the stresses are being localized in the areas with the highest curvature. In the cosine structure, this is at both the peaks and troughs of the waviness, in the arc segment and FIB determined structure, this is at only the troughs of the waviness. In the real nanolaminate structure, this localization is especially detrimental because of the porosity. Due to shading effects in the deposition process the troughs (i.e. columnar boundaries) also have a high propensity for void formation (as seen in Fig. 1). The combination of inherently weak areas due to voids along with stresses which can be larger by a factor of two than the far field stress can lead to early failure of the material.
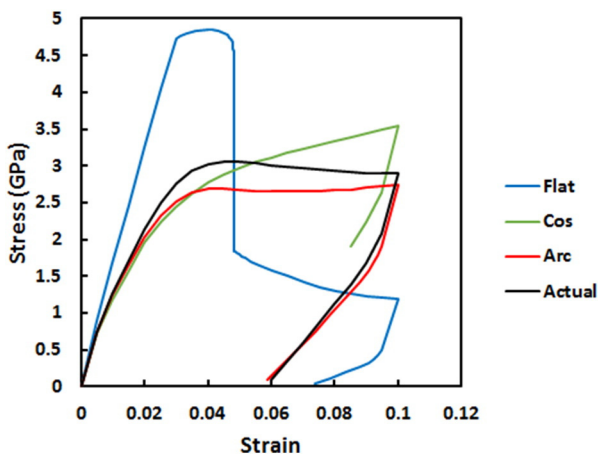

Fig. 9. Comparison of modeled responses for all four layer geometries showing that the arc structure most closely approximates the FIB derived structure.
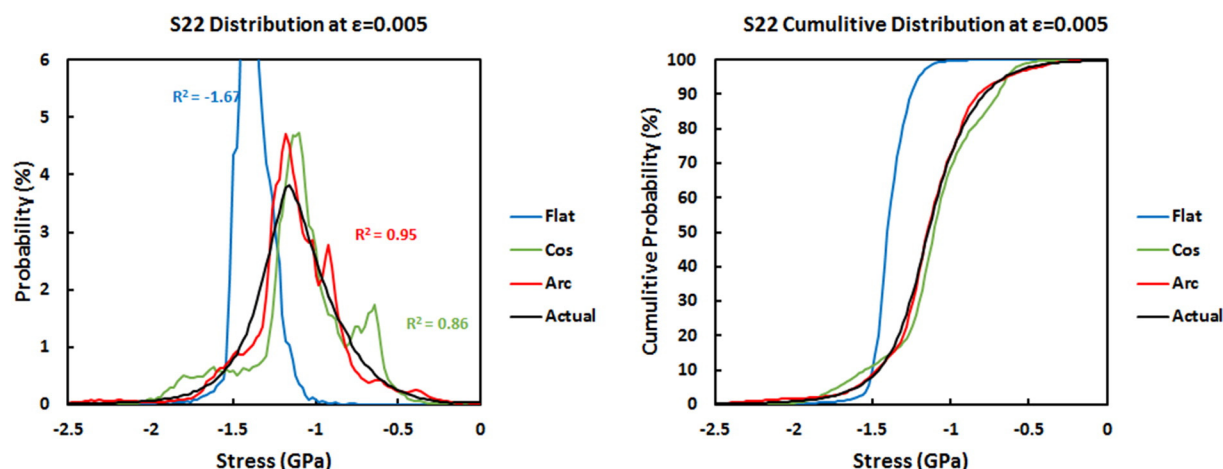
Fig. 10. Distribution and cumulative distribution of element stresses in the loading direction for each of the structures at 0.005 strain. The arc segment structure fits the results from the FIB structure the most accurately, indicating it is the most suitable for capturing how the stresses are being localized.

These weak spots in the structure can have significant effects on the mechanical properties of the laminate. For one, they can act as preexisting flaws which would explain the strong Weibull size effect observed in pillar compression [21]. The low strength of the columnar boundaries also plays a role in the fracture toughness of these materials. At small layer thicknesses (~10 nm) where plasticity in the highly constrained Al layers is low, the fracture surfaces indicate that the fracture path is dominated by propagation through columnar boundaries [32].

4. Conclusions

This work has provided insight into the role the nanostructure plays in the deformation behavior of Al-SiC nanolaminate composites allowing the following conclusions to be drawn;

- The waviness of the structure makes a significant contribution to the mechanical response of these materials and needs to be accounted for in order to obtain even qualitative agreement with experiment.
- Close agreement between experimental pillar compression and the modeled response of the FIB determined nanostructure was observed in the stress vs plastic strain behavior.
- Of the simplified structures used for modeling, the structure consisting of arc segments provided the stress strain response closest to the one obtained using the FIB tomography determined nanostructure
- The arc segment based nanostructure was also able to closely reproduce the distribution of SiC element stresses seen in the FIB tomography determined nanostructure, indicating that the stresses are localized in a similar fashion.
- The two above conclusions indicate that when quantitative modeling results are required, a layer geometry based on arc segments should be utilized.

Acknowledgements

References

[1] M. Shinn, L. Hultman, S. Barnett, Growth, structure, and microhardness of epitaxial TiN/NbN superlattices, J. Mater. Res. 7 (1992) 901–911.
[2] U. Wiklund, P. Hedenqvist, S. Hogmark, Multilayer cracking resistance in bending, Surf Coat Technol 97 (1–3) (1997) 773–778.
[3] N. Chawla, D. Singh, Y.-L. Shen, G. Tang, K. Chawla, Indentation mechanics and fracture behavior of metal/ceramic nanolaminate composites, J Mater Sci 43 (2008) 4383–4390.
[4] D. Singh, N. Chawla, Scratch resistance of Al/SiC metal/ceramic nanolaminates, J. Mater. Res. 27 (2012) 278–283.
[5] N.A. Mara, D. Bhattacharyya, P. Dickerson, R.G. Hoagland, A. Misra, Deformability of ultrahigh strength 5 nm Cu-Nb nanolayered composites, Appl Phys Lett 92 (23) (2008) 1–3.
[6] D. Singh, N. Chawla, G. Tang, Y.-L. Shen, Micropillar compression of Al/SiC nanolaminates, Acta Mater 58 (20) (2010) 6628–6636.
[7] W. Li, B. Kabius, O. Auciello, Science and technology of biocompatible thin films for implantable biomedical devices, Engineering in Medicine and Biology Society (EMBC), 2010 Annual International Conference of the IEEE 2010, pp. 6237–6242.
[8] G.S. Hickey, S.-S. Lih, T.W. Barbee Jr., Development of nanolaminate thin-shell mirrors, Proc. SPIE 4849 (2002) 63–76.
[9] Y. Wang, J. Li, A.V. Hamza, T.W. Barbee, Ductile crystalline-amorphous nanolaminates, Proc Natl Acad Sci 104 (27) (2007) 11155–11160.
[10] R. Zhang, T. Germann, J. Wang, X.-Y. Liu, I. Beyerlein, Role of interface structure on the plastic response of Cu/Nb nanolaminates under shock compression: non-equilibrium molecular dynamics simulations, Scr Mater 68 (2) (2013) 114–117.
[11] M. Liu, J. Huang, Y. Fong, S. Ju, X. Du, H. Pei, T. Nieh, Assessing the interfacial strength of an amorphous-crystalline interface, Acta Mater 61 (9) (2013) 3304–3313.
[12] N.M. Ghoniem, X. Han, Dislocation motion in anisotropic multilayer materials, Philos. Mag. 85 (24) (2005) 2809–2830.
[13] R.D. Jamison, Y.-L. Shen, Indentation and overall compression behavior of multilayered thin-film composites: Effect of undulating layer geometry, J. Compos. Mater. (2015).
[14] S. Lotfian, M. Rodriguez, K. Yazzie, N. Chawla, J. Llorca, J. Molina-Aldareguia, High temperature micropillar compression of Al/SiC nanolaminates, Acta Mater 61 (12) (2013) 4439–4451.
[15] G. Tang, Y.-L. Shen, D. Singh, N. Chawla, Indentation behavior of metal-ceramic multilayers at the nanoscale: numerical analysis and experimental verification, Acta Mater 58 (6) (2010) 2033–2044.
[16] Y. Chen, Y. Liu, C. Sun, K. Yu, M. Song, H. Wang, X. Zhang, Microstructure and strengthening mechanisms in Cu/Fe multilayers, Acta Mater 60 (18) (2012) 6312–6321.
[17] G. Zhang, T. Fan, T. Wang, H. Chen, Microstructure, mechanical and tribological behavior of MoNx/SiNx multilayer coatings prepared by magnetron sputtering, Appl Surf Sci 274 (0) (2013) 231–236.
[18] C. Mayer, L. Yang, S. Singh, H. Xie, Y.-L. Shen, J. Llorca, J. Molina-Aldareguia, N. Chawla, Orientation dependence of indentation behavior in Al-SiC nanolaminate composites, Mater Lett 168 (2016) 129–133.
[19] N. Verma, V. Jayaram, Role of interface curvature on stress distribution under indentation for ZrN/Zr multilayer coating, Thin Solid Films 571 (Part 2, no. 0) (2014) 283–289 (multilayers 2013).
[20] G.S. Bales, A. Zangwill, Macroscopic model for columnar growth of amorphous films by sputter deposition, J. Vac. Sci. Technol. A 9 (1) (1991) 145–149.
[21] C. Mayer, L. Yang, S. Singh, J. Llorca, J. Molina-Aldareguia, Y. Shen, N. Chawla, Anisotropy, size, and aspect ratio effects on micropillar compression of Al-SiC nanolaminate composites, Acta Mater 114 (2016) 25–32.
[22] R. Jamison, Y.-L. Shen, Indentation behavior of multilayered thin films: Effects of layer undulation, Thin Solid Films 570 (Part B) (2014) 235–242 (2013 International Thin Films Conference).

[23] N. Chawla, B. Patel, M. Koopman, K. Chawla, R. Saha, B. Patterson, E. Fuller, S. Langer, Microstructure-based simulation of thermomechanical behavior of composite materials by object-oriented finite element analysis, Mater Charact 49 (5) (2003) 395–407.

[24] M.S. Qidwai, A.C. Lewis, A.B. Geltmacher, Using image-based computational modeling to study microstructure-yield correlations in metals, Acta Mater 57 (14) (2009) 4233–4247.

[25] N. Chawla, R. Sidhu, V. Ganesh, Three-dimensional visualization and microstructure-based modeling of deformation in particle-reinforced composites, Acta Mater 54 (6) (2006) 1541–1548.

[26] R. Sidhu, N. Chawla, Three-dimensional (3D) visualization and microstructure-based modeling of deformation in a Sn-rich solder, Scr Mater 54 (9) (2006) 1627–1631.

[27] S.S. Singh, J.J. Williams, T.J. Stannard, X. Xiao, F.D. Carlo, N. Chawla, Measurement of localized corrosion rates at inclusion particles in AA7075 by in situ three dimensional (3d) x-ray synchrotron tomography, Corros Sci 104 (2016) 330–335.

[28] J. Weber, J. Barthel, F. Brandt, M. Klinkenberg, U. Breuer, M. Kruth, D. Bosbach, Nano-structural features of barite crystals observed by electron microscopy and atom probe tomography, Chem Geol 424 (2016) 51–59.

[29] D. Singh, N. Chawla, Y.-L. Shen, Focused ion beam (FIB) tomography of nanoindentation damage in nanoscale metal/ceramic multilayers, Mater Charact 61 (4) (2010) 481–488.

[30] G. Tang, Y.-L. Shen, D. Singh, N. Chawla, Indentation behavior of metal-ceramic multilayers at the nanoscale: numerical analysis and experimental verification, Acta Mater 58 (6) (2010) 2033–2044.

[31] J.R. Greer, W.C. Oliver, W.D. Nix, Size dependence of mechanical properties of gold at the micron scale in the absence of strain gradients, Acta Mater 53 (6) (2005) 1821–1830.

[32] C. Mayer, L. Yang, V. Carollo, J. Llorca, J. Molina-Aldareguia, N. Chawla, Microcantilever Bending Experiments in Al-SiC Nanolaminate Composites: Characterization of Tension-Compression Asymmetry and Fracture Toughness as a Function of Crack Orientation and Layer Thickness, 2016 (Unpublished Manuscript).